Calorimetry at a Future Linear Collider

Steven Green
of Emmanuel College

A dissertation submitted to the University of Cambridge
for the degree of Doctor of Philosophy

Abstract

This thesis describes the optimisation of the calorimeter design for collider experiments at the future Compact LInear Collider (CLIC) and the International Linear Collider (ILC). The detector design of these experiments is built around high-granularity Particle Flow Calorimetry that, in contrast to traditional calorimetry, uses the energy measurements for charged particles from the tracking detectors. This can only be realised if calorimetric energy deposits from charged particles can be separated from those of neutral particles. This is made possible with fine granularity calorimeters and sophisticated pattern recognition software, which is provided by the PandoraPFA algorithm. This thesis presents results on Particle Flow calorimetry performance for a number of detector configurations. To obtain these results a new calibration procedure was developed and applied to the detector simulation and reconstruction to ensure optimal performance was achieved for each detector configuration considered.

This thesis also describes the development of a software compensation technique that vastly improves the intrinsic energy resolution of a Particle Flow Calorimetry detector. This technique is implemented within the PandoraPFA framework and demonstrates the gains that can be made by fully exploiting the information provided by the fine granularity calorimeters envisaged at a future linear collider.

A study of the sensitivity of the CLIC experiment to anomalous gauge couplings that effect vector boson scattering processes is presented. These anomalous couplings provide insight into possible beyond standard model physics. This study, which utilises the excellent jet energy resolution from Particle Flow Calorimetry, was performed at centre-of-mass energies of 1.4 TeV and 3 TeV with integrated luminosities of $1.5 \mathrm{ab}^{-1}$

and 2ab^{-1} respectively. The precision achievable at CLIC is shown to be approximately one to two orders of magnitude better than that currently offered by the LHC.

In addition, a study into various technology options for the CLIC vertex detector is described.

Declaration

This dissertation is the result of my own work, except where explicit reference is made to the work of others, and has not been submitted for another qualification to this or any other university. This dissertation does not exceed the word limit for the respective Degree Committee.

Steven Green

Acknowledgements

Of the many people who deserve thanks, some are particularly prominent, such as my supervisor. . .

Contents

x

*"Writing in English is the most ingenious torture
ever devised for sins committed in previous lives."*
— James Joyce

Chapter 1

Calorimeter Optimisation Studies

"The simple believes everything, but the prudent gives thought to his steps."
— Proverbs 14:15

1.1 Introduction

This chapter describes the optimisation of the calorimeters used at the linear collider, with focus placed on obtaining the best energy resolution for jets. Parameters such as the number of layers, cell size and material choices for the calorimeters are investigated. Several global detector parameters such as the magnetic field strength and the inner radius of the ECal are also studied. These parameters are not calorimeter specific, but affect the jet energy resolution obtained from particle flow.

1.2 Electromagnetic Calorimeter Optimisation

The purpose of an electromagnetic calorimeter (ECal) is to measure the energy deposits from electromagnetic showers. The nominal ILD ECal, summarised in table 1.1, is a silicon-tungsten sampling calorimeter. It contains 29 readout layers and 24 radiation lengths (X_0), which is sufficient to contain all but the highest energy electromagnetic showers. The absorber thickness of the last nine layers is twice that of the first 20 layers to reduce the number of readout channels and cost of the calorimeter. The high

longitudinal sampling frequency is crucial for the pattern recognition aspect of particle flow calorimetry, especially in the region where particle showers start developing.

Parameter	Default Value
Cell Size	5×5 mm^2 square cells
Number of Layers	29 readout layers
Active Material Choice	Silicon or Scintillator
Active Material Thickness	0.5 mm (Silicon) or 2 mm (Scintillator)
Absorber Material Choice	Tungsten
Absorber Material Thickness	20 layers of 2.1 mm followed by 9 layers of 4.2 mm

Table 1.1: The configuration of the silicon and scintillator ECal options for the ILD detector model [1].

The calorimeter performance was simulated for a number of detector models where the following detector parameters were varied:

- Cell size: This is a vital aspect of the detector in the particle flow paradigm as smaller cell sizes leads to better separation between nearby showering particles, which helps to minimise the effect of confusion. Modifying the cell size should have little effect on the intrinsic energy resolution of the detector.

- Longitudinal sampling frequency: The longitudinal sampling frequency in the ECal was varied by changing the number of layers in the ECal while simultaneously changing the thicknesses of the layers such that the total depth, in radiation lengths, was held constant. Increasing the number of layers in a sampling calorimeter means any particles showering within it are sampled more, which leads to a reduction in the stochastic contribution to the energy resolution. Therefore, varying the number of layers is expected to change in intrinsic energy resolution of the calorimeter.

- Active material choice: The options under consideration for the active sensor material are silicon or plastic scintillator. As well as providing different intrinsic energy resolutions the readout mechanics of these two options are significantly different. There is no clear prior knowledge as to which should provide better performance.

1.2.1 ECal Cell Size

Different detector models were considered where the cell size in the ECal was varied about the nominal value of 5×5 mm^2 square cells. The granularities considered were 3×3 mm^2, 5×5 mm^2, 7×7 mm^2, 10×10 mm^2, 15×15 mm^2 and 20×20 mm^2 square cells for both the silicon and scintillator active material options.

The energy resolution, using 100 GeV γ events, as a function of the ECal cell size is shown in figure 1.2a for the silicon option and in figure 1.2b for the scintillator option. At this energy, the γs will be largely contained within the ECal and the reported energy resolution reflects solely the performance of the ECal. For both the silicon and scintillator ECal options the energy resolution does not depend strongly on the ECal cell size. This is to be expected as there is no change in the number of layers, which is the main factor in determining the energy resolution of a sampling calorimeter.

The only statistically significant variation observed occurs for the scintillator ECal option. A degradation in the energy resolution of $\sim 10\%$ is observed when reducing the ECal cell size from 5×5 mm^2 to 3×3 mm^2. The most likely cause is the "dead" region in the active material, which represents the readout multi pixel photon counter (MPPC) [2]. The MPPC occupies a fixed area of the cell, irrespective of cell size, and so the dead region of the cell fractionally increases as cell size is reduced. The larger this dead region, the worse the sampling of the electromagnetic showers in the ECal and the worse the resolution. While this effect will be present in all scintillator ECal options, it will only be significant for the small cell sizes when the dead region is fractionally the largest.

The ability to separate nearby electromagnetic particle showers within a calorimeter is limited by the Moliére radius of the absorber material and the cell size. The Moliére radius controls the width of the electromagnetic shower, while the cell size controls how the transverse shower profile is sampled. By reducing the cell size, it becomes easier to resolve nearby electromagnetic showers, which in turn reduces the effect of confusion. Therefore, it is expected that the jet energy resolution will be sensitive to the ECal cell size, even though the intrinsic energy resolution is not. The jet energy resolution as a function of ECal cell size is shown in figure 1.2a for the silicon option and figure 1.2b for the scintillator option. As expected, there is a strong dependance on the ECal cell size, with smaller cell sizes leading to lower values of the jet energy resolution. The origin of this trend is best illustrated by considering the intrinsic energy resolution and confusion contributions to the jet energy resolution. These contributions are shown as a function
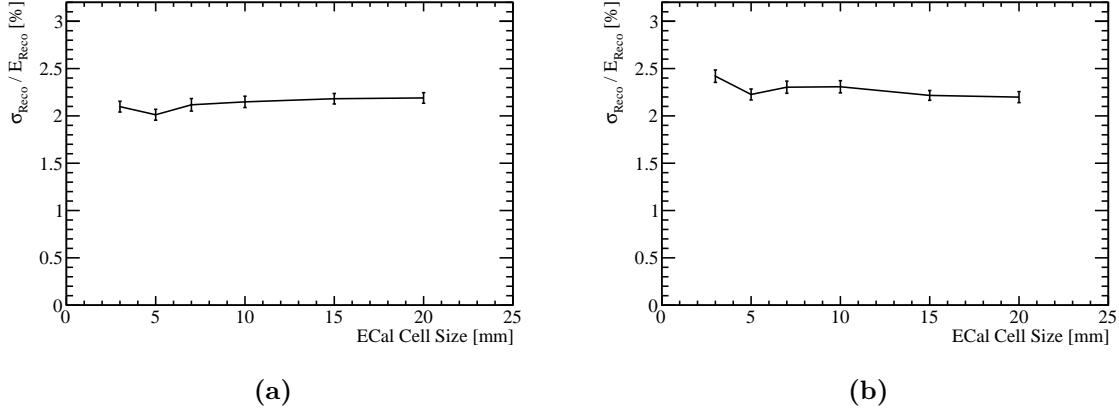
Figure 1.1: The energy resolution as a function of ECal cell size for 100 GeV γs using the nominal ILD detector model with (a) the silicon and (b) the scintillator ECal option.

of ECal cell size for 45 and 250 GeV jets in figure 1.3. It is clear from these contributions that the intrinsic energy resolution of the detector does not change when varying the cell size, which agrees with both prior expectations of calorimeter behaviour and the single particle energy resolution study. As expected, it can be seen that the trend in jet energy resolution as a function of the ECal cell size is being driven purely by changes to the confusion contribution and, in particular, the confusion caused by the reconstruction of γs.
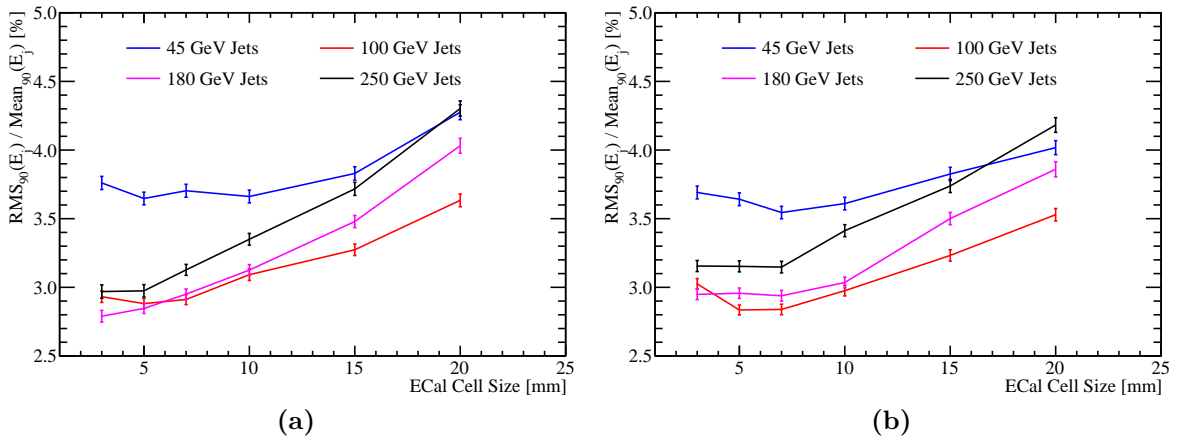

Figure 1.2: The fractional jet energy resolution as a function of ECal cell size for various jet energies using the nominal ILD detector model with (a) the silicon and (b) the scintillator ECal option.
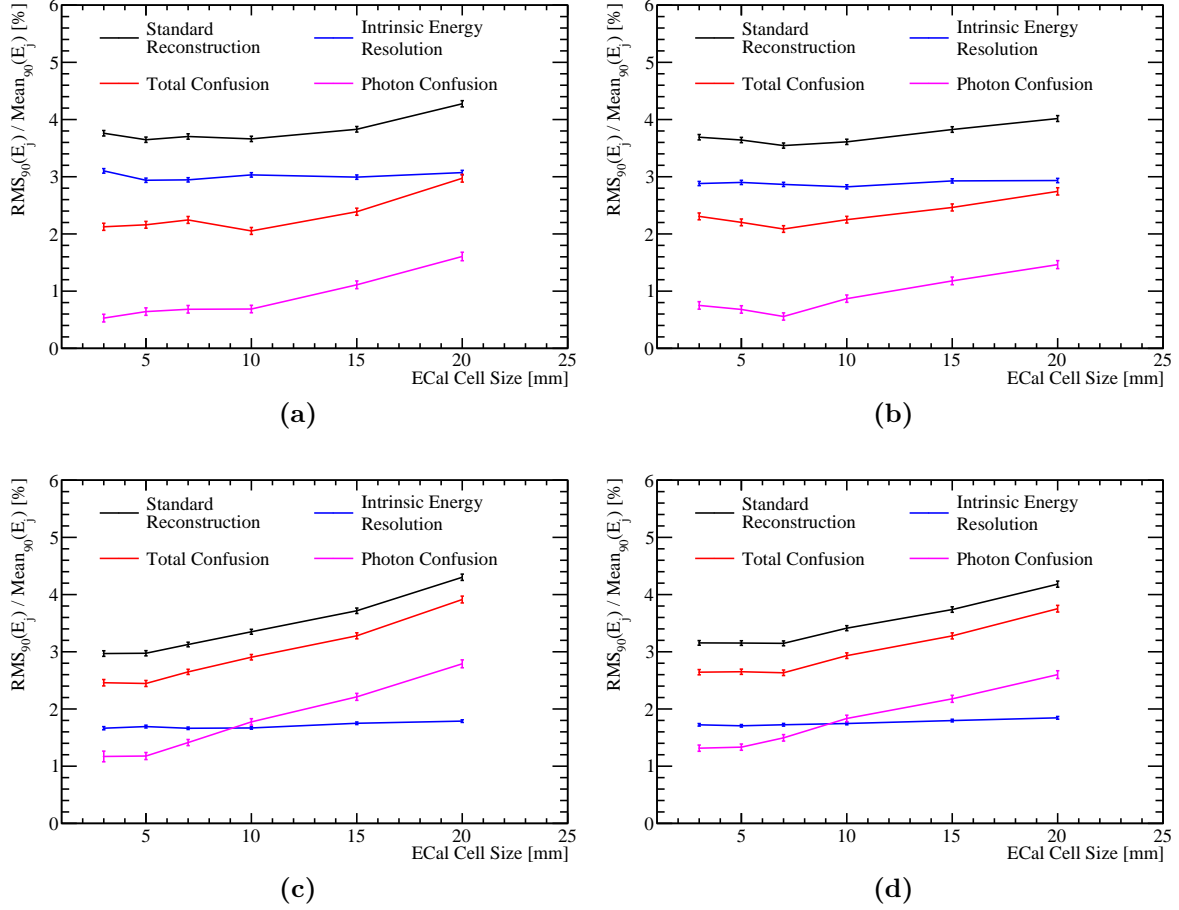
Figure 1.3: The contributions to the jet energy resolution as a function of ECal cell size using the nominal ILD detector model for (a) the silicon ECal option and 45 GeV jets, (b) the scintillator ECal option and 45 GeV jets, (c) the silicon ECal option and 250 GeV jets and (d) the scintillator ECal option and 250 GeV jets. The black curves correspond to the standard reconstruction, the blue curves to the intrinsic energy resolution contribution to the jet energy resolution, the red curves to the confusion contribution to the jet energy resolution and the magenta curves to the confusion contribution to the jet energy resolution related solely to γ reconstruction

It is clear that the ECal cell size is extremely important for jet energy measurements, although it has little bearing on the intrinsic energy resolution of the ECal. Separation of the hadronic decays of the W and Z bosons, i.e. $\sigma_E/E \lesssim 3.8\%$, can be achieved across the jet energy range considered here using a maximum ECal cell size of 15×15 mm^2. However, as reducing the ECal cell size further continues to benefit the jet energy resolution, minimising the ECal cell size is desirable.

1.2.2 ECal Longitudinal Sampling Frequency

The detector performance was simulated where the number of layers in the ECal was varied, while keeping the total material budget (X_0) approximately constant. This study was performed for both the silicon and scintillator active material options. In all cases tungsten was used for the ECal absorber material and the active layer thicknesses were not changed from those used in the nominal ILD ECal summarised in table 1.1. The different ECal layouts considered are summarised in table 1.2.

Total Number of Layers $N_{\text{Layers ECal}}$	N_{Layers} Region 1	Absorber Thickness Region 1 [mm]	N_{Layers} Region 2	Absorber Thickness Region 2 [mm]	Total Thickness [X_0]
30	20	2.10	9	4.20	22.77
26	17	2.40	8	4.80	22.60
20	13	3.15	6	6.30	22.47
16	10	4.00	5	8.00	22.31

Table 1.2: The longitudinal structure of the ECal models considered in the optimisation study. The radiation length of tungsten absorber is 3.504 mm [3]. Note that a presampler layer contributes one extra layer to the cumulative number of layers.

The energy resolution, for 100 GeV γ events, as a function of the number of layers in the ECal is shown in figure 1.4a for the silicon option and in figure 1.4b for the scintillator option. When the number of layers is increased σ_E/E decreases, which is expected because the energy resolution for a sampling calorimeter is $\propto 1/\sqrt{E \times N_{Layers}}$, where E is the reconstructed energy and N_{Layers} is the number of layers in the calorimeter.

When the number of layers in the ECal is increased, the intrinsic energy resolution of the ECal improves. This has the knock-on effect of reducing the confusion contribution to the jet energy resolution, which can be seen in figures 1.5a and 1.5b for the silicon and scintillator ECal options respectively. In both cases, the jet energy resolution was found to improve when the number of layers in the ECal was increased. The magnitude of the change in jet energy resolution is dependent upon the jet energy, with a stronger dependancy being observed for low energy jets. This is expected from the stochastic contribution to the energy resolution for a sampling calorimeter. For high jet energies, changing the number of layers in the ECal does not significantly affect the jet energy resolution because the jet energy resolution is dominated by confusion. For low jet
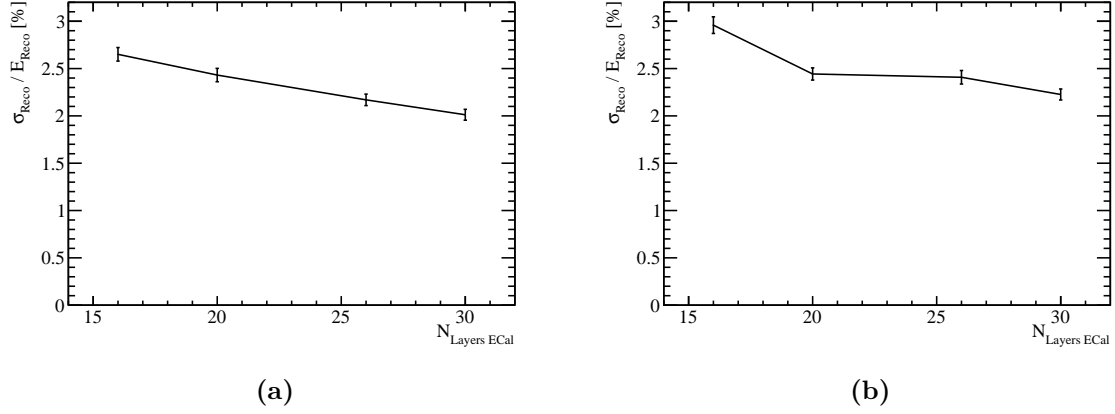
Figure 1.4: The energy resolution as a function of number of layers in the ECal for 100 GeV γs using the nominal ILD detector model with (a) the silicon and (b) the scintillator ECal option.

energies, the stochastic contribution to the energy resolution is bigger making it possible to resolve the changes to it when varying the number of layers in the ECal.

The decomposition of the jet energy resolution into the intrinsic energy resolution and confusion contributions for 45 and 250 GeV jets are shown, for both the silicon and scintillator ECal options, in figure 1.6. As expected, the improvement to the intrinsic energy resolution seen when increasing the number of layers in the ECal leads to the knock-on effect of lowering the confusion. However, significantly the magnitude of the change to the intrinsic energy resolution and confusion contributions to the jet energy resolution when varying the number of layers in the ECal are comparable in size. This shows that pattern recognition is as important for detector performance in the particle flow paradigm than intrinsic energy resolution.

1.2.3 ECal Active Material

In sections 1.2.1 and 1.2.2 the performance of the ECal was reported for both the silicon and scintillator options and to a large extent the performance of the two options was similar, but not identical:

- The intrinsic energy resolution of the silicon ECal option is better than that of the scintillator option for high energies. Section **??** contains a comparison between the photon energy resolution for the two ECal options, which most clearly illustrates this point. The most likely origin of the differing energy resolutions is the implementation
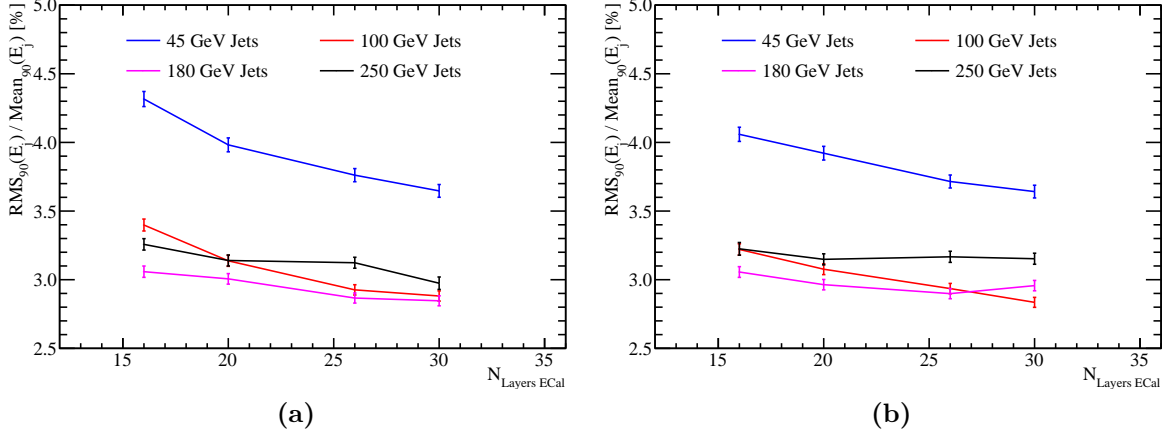
Figure 1.5: The jet energy resolution as a function of number of layers in the ECal for various jet energies using the nominal ILD detector model with (a) the silicon and (b) the scintillator ECal option.

of Birks' law [4] for scintillator active materials, which states

$$d\mathcal{L}/dx \propto \frac{dE/dx}{1 + k_B dE/dx} \, , \tag{1.1}$$

where $d\mathcal{L}/dx$ is the scintillation light yield per unit path length, dE/dx is the energy deposited per unit path length and k_B is a material property constant. For large energy deposits per unit length, such as those found in high energy γ events, the light yield saturates causing a degradation in the energy resolution. When comparing the photon energy resolution for the silicon and scintillator ILD ECal options, which can be found in section **??**, the saturation effect starts to degrade the energy resolution for the scintillator option around 50 GeV. However, the degradation in energy resolution is relatively small event up to 100 GeV.

- The "dead" region due to the presence of the MPPC in the simulation of the scintillator ECal option degrades performance of the detector for small transverse granularities, see figure 1.1.

In summary, the performance of the two options, in terms of energy and jet energy resolution, are similar, meaning no clear option is preferred. However, the silicon option is preferred when manufacture and implementation of the two models is compared. While constructing silicon wafers to fit a 5×5 mm^2 square cell size is achievable, this would be extremely challenging for scintillator tiles. To resolve this in actuality, the scintillator ECal option would have to use 5×45 mm^2 scintillator strips that are arranged
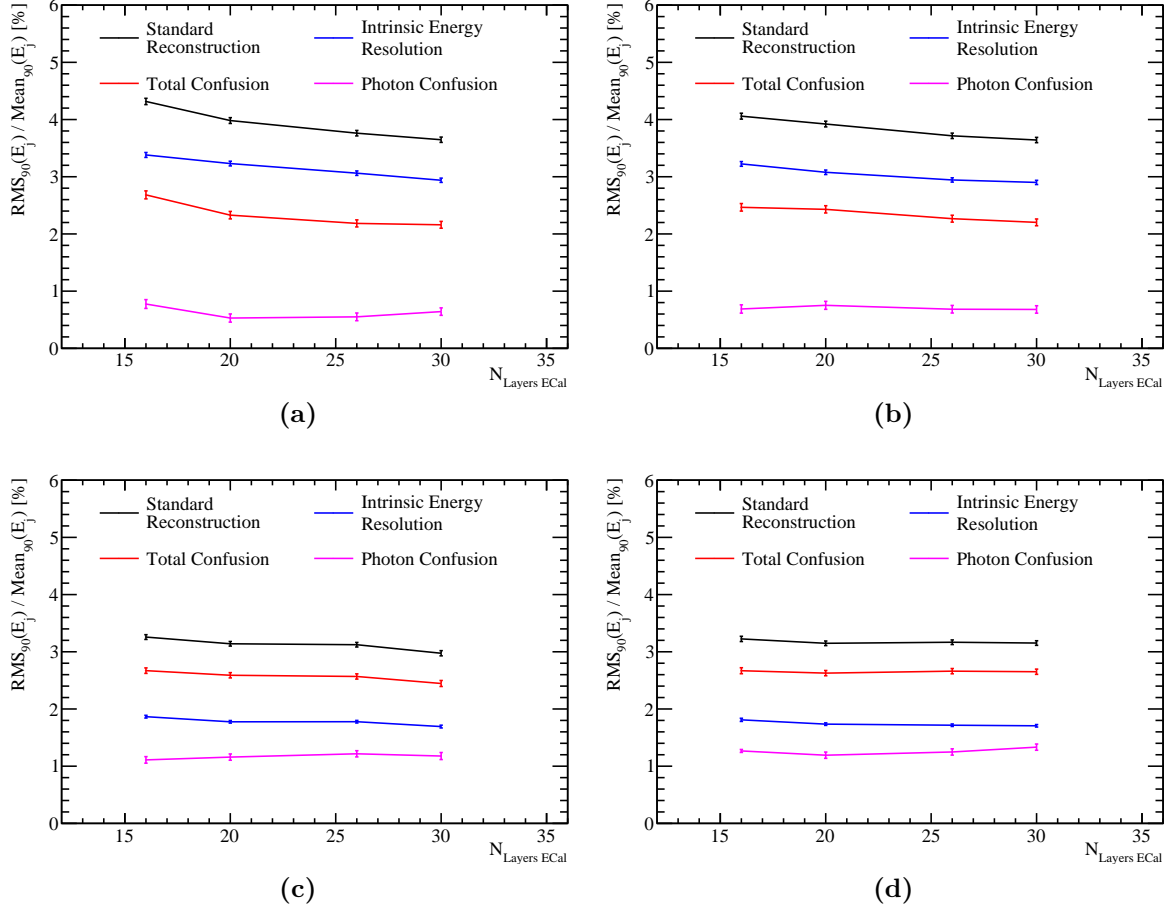
Figure 1.6: The contributions to the jet energy resolution as a function of number of layers in the ECal using the nominal ILD detector model for (a) the silicon ECal option and 45 GeV jets, (b) the scintillator ECal option and 45 GeV jets, (c) the silicon ECal option and 250 GeV jets and (d) the scintillator ECal option and 250 GeV jets. The black curves correspond to the standard reconstruction, the blue curves to the intrinsic energy resolution contribution to the jet energy resolution, the red curves to the confusion contribution to the jet energy resolution and the magenta curves to the confusion contribution to the jet energy resolution related solely to γ reconstruction.

in alternating directions in each ECal layer. By combining information from neighbouring layers it becomes possible to approach an effective 5×5 mm^2 square cell size.

1.3 Hadronic Calorimeter Optimisation

The purpose of an hadroinc calorimeter (HCal) is to measures the energy deposits from hadronic showers. The HCal in the default ILD detector model, summarised in table 1.3, is approximately 6 nuclear interaction lengths (λ_I) deep. The ECal contributes approximately one λ_I giving a total of $\approx 7\lambda_I$, which is sufficient to contain jets at ILC like energies. The longitudinal structure of this model consists of 48 readout layers each containing a 3 mm active layer of scintillator and a 20 mm absorber layer of iron.

Parameter	Default Value
Cell Size	30×30 mm^2 square cells
Number of Layers	48 readout layers
Active Material Choice	Scintillator
Active Material Thickness	3 mm
Absorber Material Choice	Steel
Absorber Material Thickness	20 mm

Table 1.3: The configuration of the HCal in the nominal ILD detector model [1].

There are several readout approaches under consideration for the HCal including fully analogue, fully digital and semi-digital. Analogue readout reports the energy within each HCal cell using a continuous variable, while digital readout only produces a response if the energy deposited within a calorimeter cell is above a given threshold. The semi-digital approach mirrors that of the digital approach, but has three responses each with a different energy threshold. While the energy resolution for digital calorimeters is not as good as that of analogue calorimeters, it is possible to construct smaller cell sizes using a digital readout. In traditional calorimetry, a digital calorimeter would give a worse jet energy resolution than the analogue equivalent, however, that is not necessarily the case in particle flow calorimetry. If a digital calorimeter could be realised with a much small cell size than the analogue equivalent, then the affect of confusion in the digital calorimeter may be reduced such that it compensates for any loss to intrinsic energy resolution. In the following studies only the optimisation of the analogue HCal is presented as this is the readout approach used in the nominal ILD detector model.

A number of options were simulated where the following parameters in the HCal were varied:

- Cell size: This is crucial for successful application particle flow calorimetry for making associations between clusters of calorimeter hits and charged particle tracks. It is expected that the intrinsic energy resolution be invariant to changes in the HCal cell size.

- Number of readout layers: The number of layers in the HCal are varied, however, the thickness of those layers match those of the nominal ILD HCal design. This means the total depth of the HCal in λ_I is changing. It is expected that this study will determine the effect of leakage of energy out of the back of the HCal.

- Longitudinal sampling frequency: This involves changing the number of readout layers in the HCal while simultaneously changing the thicknesses of the active and absorber layers to keep the total number of λ_I in the HCal constant. As this modifies the sampling of particle showers in the HCal, it will affect the intrinsic energy resolution of the HCal.

- Sampling fraction: This is the ratio of the active medium thickness to the absorber medium thickness. This controls how particle showers within the calorimeter are sampled. In this study the total depth of the HCal in λ_I is held constant between detector models.

- Absorber material choice: Two options have been considered: steel and tungsten. This choice affects the growth and propagation of hadronic showers.

1.3.1 HCal Cell Size

The HCal cell size is an important detector parameter in the application of particle flow calorimetry. Smaller HCal cell sizes will lead to a finer spatial resolution that can be used to better separate charged and neutral particle calorimetric energy deposits. On the other hand, this will also lead to an increase in the number of readout channels that will raise the cost of the calorimeter. Therefore, it is highly desirable to achieve the optimal physics performance using the largest cell size possible. The nominal ILD HCal has a 30 mm square cell size and in this study the following cell sizes were considered; 10×10 mm^2, 20×20 mm^2, 30×30 mm^2, 40×40 mm^2, 50×50 mm^2 and 100×100 mm^2.

Figure 1.7 shows the energy resolution for 50 GeV K_L^0 events as a function of cell size. These K_L^0 samples will deposit energy primarily within the HCal, making them appropriate events to consider when determining the performance of the HCal. However,

a non-neglibile amount of energy will also be deposited within the ECal. Therefore, these energy resolutions represent the intrinsic energy resolution of the ILD detector as a whole and not purely that of the HCal. It is clear that the hadronic energy resolution is not strongly dependent on the HCal cell size. The only statistically significant variation in energy resolution is observed for the 100×100 mm^2 HCal cell size. For this model the energy resolution gets gets worse by $\sim 8\%$ in comparison to the other models considered. The most likely cause of this is a reduction in the effectiveness of the HCal hit energy truncation, which is described in section **??**. The reduced effectiveness is expected because the precision used when obtaining the optimal energy truncation becomes worse as HCal cell size diverges from the nominal value.
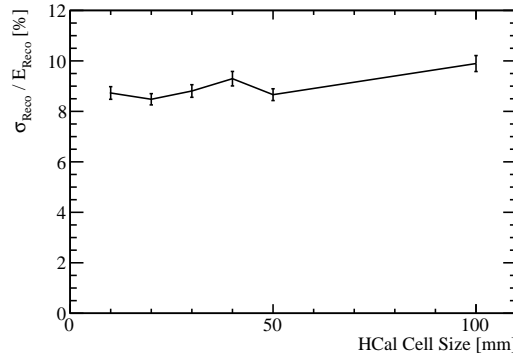

Figure 1.7: The energy resolution as a function of HCal cell size for 50 GeV K_L^0 events using the nominal ILD detector model.

A smaller HCal cell size will lead to better separation of charged and neutral hadron calorimetric energy deposits, therefore, it is expected that the confusion contribution to the jet energy resolution will be reduced by using smaller HCal cell sizes. Figure 1.8 shows the jet energy resolution as a function of cell size in the HCal. At low jet energies there is no strong dependency of the jet energy resolution on the HCal cell size, which is as expected from the K_L^0 energy resolution study. For high energy jets there is a clear dependence, with lower HCal cell sizes leading to better jet energy resolutions. Examining the different contributions to the jet energy resolution, shown in figure 1.9 it can be seen that the intrinsic energy resolution contribution does not depend on the HCal cell size; it is the confusion contribution that drives the overall trend in the jet energy resolution. This is particularly clear at high jet energies where the confusion contribution to the jet energy resolution dominates that of the intrinsic energy resolution contribution. At high jet energies smaller HCal cell sizes leads to a reduction in the effect of confusion. At low jet energies the trend is less clear, as the confusion contribution is

less dominant. Nevertheless, a reduction in the effect of confusion with decreasing cell size is still visible for all but the smallest HCal cell size. The most likely cause of the increase in confusion for the smallest HCal cell size at low energies is the tuning of the PandoraPFA algorithms to the nominal ILD HCal cell size. For both the 45 and 250 GeV jets, the photon confusion does not depend on the HCal cell size. This indicates that changes to the confusion term seen when varying the HCal cell size are related solely to the reconstruction of hadrons. onty135
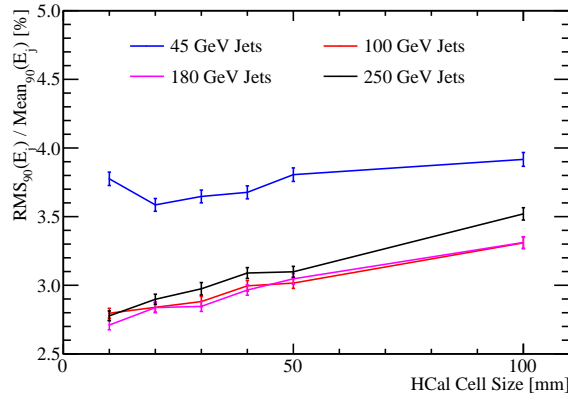

Figure 1.8: The jet energy resolution as a function of HCal cell size for various jet energies using the nominal ILD detector model.
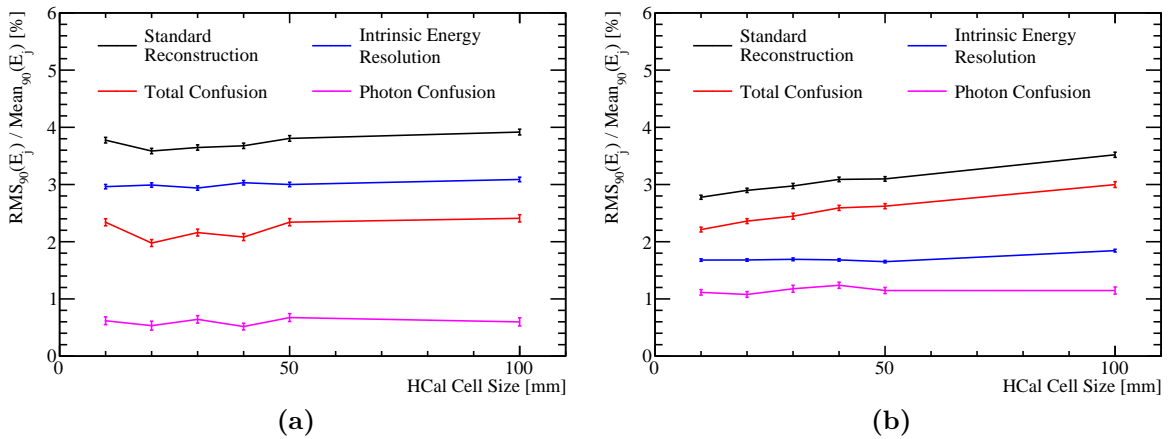

Figure 1.9: The contributions to the jet energy resolution as a function of HCal cell size using the nominal ILD detector model for (a) 45 GeV jets and (b) 250 GeV jets. The black curves correspond to the standard reconstruction, the blue curves to the intrinsic energy resolution contribution to the jet energy resolution, the red curves to the confusion contribution to the jet energy resolution and the magenta curves to the confusion contribution to the jet energy resolution related solely to γ reconstruction.

A comparison of the results from the ECal and HCal cell size optimisation studies shows that the jet energy resolution has a much stronger dependency on the ECal cell size than on the HCal cell size. This is to be expected as in the particle flow paradigm $\approx 30\%$ of jet energy is recorded in the ECal, while only $\approx 10\%$ is recorded in the HCal. Consequently, the potential effect of double counting and omitting energy deposits, i.e. confusion, is greater in the ECal than the HCal. Therefore, minimising confusion in the ECal is expected to be more crucial for the overall jet energy resolution, which is what is observed. Furthermore, as PandoraPFA groups calorimeter hits together using a cone clustering approach, identifying the start of a particle shower is key for determining how calorimeter hits are grouped together deeper into the calorimeters. In effect, this means the grouping of calorimeter hits in the HCal depends upon information gathered in the ECal. Therefore, if the ECal performance is sufficiently good, even with coarse HCal cell sizes, excellent performance can be achieved.

In summary, the confusion contribution to the jet energy resolution falls as the HCal cell size is reduced, while the intrinsic energy resolution of the detector is largely unaffected. As this dependancy is relatively weak, even the use of 100×100 mm^2 HCal cell sizes would be enough to allow for separation of the hadronic decays of W and Z bosons, i.e. $\sigma_E/E \lesssim 3.8\%$, at ILC like energies. However, there are benefits to having smaller HCal cell size; the jet energy resolution is reduced from $\sim 3.5\%$ to $\sim 2.8\%$ for 250 GeV jets when decreasing the HCal cell size from 100×100 mm^2 to 10×10 mm^2.

1.3.2 HCal Number of Layers

In this study, the total number of layers in the HCal was varied. In contrast to the longitudinal sampling frequency study, the active and absorber layer thicknesses in the HCal were not altered. Changing the number of layers in this way leads to a change in the total thickness of the calorimeter. This study is sensitive to the effects, if any, of leakage of energy out of the back of the calorimeters. The manufacturing cost of the HCal is proportional to the number of readout channels and layers. Therefore, minimising the number of layers, while retaining excellent physics performance is important. Here detector models were simulated with a HCal containing 36, 42, 48 (nominal), 54 and 60 layers.

It is expected that the energy resolution of the detector will improve when the number of layers in the HCal is increased since fewer events should suffer from the effects of leakage. Any improvements seen by increasing the number of layers in the HCal is

expected only up to the point where the majority of hadronic showers are fully contained by the calorimeters. The energy resolution as a function of number of layers in the HCal for 50 GeV K_L^0 is shown in figure 1.10. The energy resolution becomes worse as the number of layers in the HCal is reduced below 48 layers, while above this point additional layers do not change the energy resolution. This indicates that the majority of hadronic showers at this energy are fully contained by a 48 layer HCal. As reducing the number of HCal layers to 36 only causes a small degradation in the neutral hadron energy resolution, it is feasible to consider reducing the number of layers in the ILD HCal.
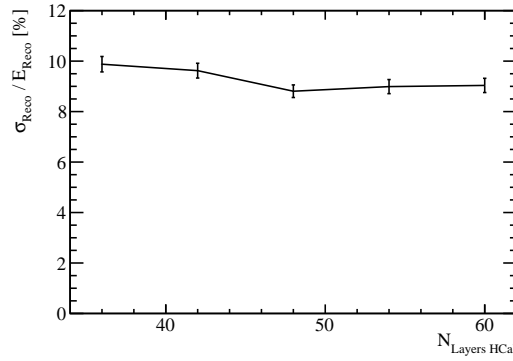
Figure 1.10: The energy resolution as a function of number of layers in the HCal for 50 GeV K_L^0 events using the nominal ILD detector model.

Figure 1.11 shows the jet energy resolution as a function of the number of layers in the HCal. For low energy jets, where intrinsic energy resolution dominates, the jet energy resolution is does not depend on the number of layers in the HCal. At high jet energies, where confusion dominates, increasing the number of layers in the HCal improves the jet energy resolution; the jet energy resolution is goes from $\sim 3.4\%$ to $\sim 3.0\%$ for 250 GeV jets when increasing the number of HCal layers from 36 to 48. The origin of these trends is leakage of energy out of the back of the calorimeters, which becomes more problematic as the number of layers in the HCal is reduced and the jet energy increases.

Figure 1.12 shows the jet energy resolution contributions as a function of the number of layers in the HCal. These results appear somewhat counterintuitive in that the intrinsic energy resolution of the detector does not seem to depend on the number of layers in the HCal even for high energy jets. However, this is expected given only 10% of jet energy is carried in the form of neutral hadrons and the neutral hadron energy resolution, for 50 GeV hadrons, is only weakly dependent on the number of HCal layers. Leakage does have an effect on the intrinsic jet energy resolution, however, the use of RMS_{90} obscures part of this by excluding events where leakage is significant. The fractional decrease

in RMS_{90} for the intrinsic jet energy distribution when increasing the number of HCal layers from 36 to 60 is $\sim 4\%$, however, the change in the full RMS is $\sim 23\%$. Figure 1.12 also shows that the confusion contribution is far more sensitive to the number of layers in the HCal than the intrinsic energy resolution. This sensitivity originates from the reclustering stage of the reconstruction in events where leakage has occurred. In these events, when PandoraPFA compares the momentum of a charged particle track to the cluster of calorimeter hits that it produces, there will be a disparity. To resole the disparity, PandoraPFA will associate other calorimeter energy deposits that were not produced by the charged particle to the track to compensate for the leaked energy, which produces confusion. As photons are largely contained within the ECal at these energies, the photon confusion contribution to the jet energy resolution has no dependence on the number of layers in the HCal.
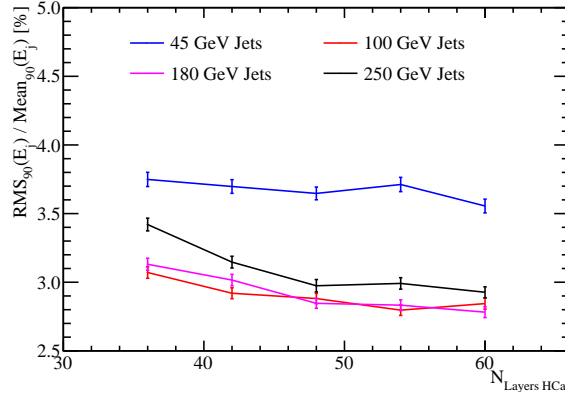

Figure 1.11: The jet energy resolution as a function of number of layers in the HCal for various jet energies using the nominal ILD detector model.

In summary, even if the number of layers in the HCal were reduced by 25%, the jet energy resolution would be sufficient for separating the hadronic decays of the W and Z bosons at ILC energies, i.e. $\sigma_E/E \lesssim 3.8\%$. Although, the effects of leakage do make the jet energy resolution worse for ILC like energies, once the number of layers in the HCal is reduced from 48 layers, therefore, it is desirable to have a minimum of 48 layers in the ILD HCal.

1.3.3 HCal Longitudinal Sampling Frequency

Several detector models were simulated where the longitudinal sampling frequency in the HCal was modified. The longitudinal sampling frequency was altered by changing the number of layers in the HCal, while simultaneously changing the active and absorber
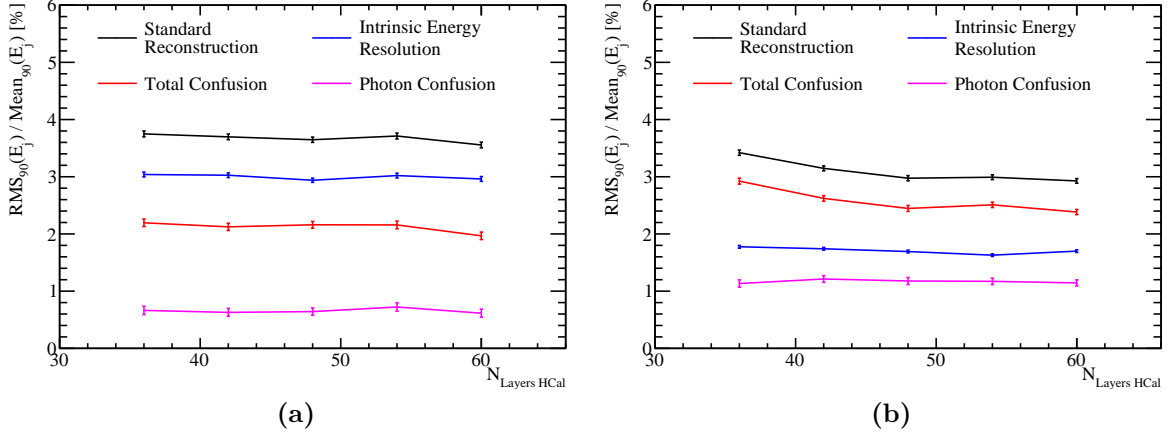
Figure 1.12: The contributions to the jet energy resolution as a function of number of layers in the HCal using the nominal ILD detector model for (a) 45 GeV jets and (b) 250 GeV jets. The black curves correspond to the standard reconstruction, the blue curves to the intrinsic energy resolution contribution to the jet energy resolution, the red curves to the confusion contribution to the jet energy resolution and the magenta curves to the confusion contribution to the jet energy resolution related solely to γ reconstruction.

layer thicknesses, to maintain the total number of nuclear interaction lengths in the HCal. For each model considered, the absorber material was steel, containing a total of 5.72 λ_I, and the active material was scintillator, containing a total of 0.19 λ_I. The ratio of the active to absorber layers thicknesses (the sampling fraction) in these models is the same as in the nominal ILD HCal. A summary of the detector models considered is given in table 1.4.

Number $N_{\text{Layers HCal}}$	Absorber Thickness [mm]	Active Thickness [mm]
60	16.00	2.40
54	17.78	2.67
48	20.00	3.00
42	22.86	3.43
36	26.67	4.00
30	32.00	4.80
24	40.00	6.00
18	53.33	8.00

Table 1.4: Longitudinal configuration of the HCal in the detector models considered.

Figure 1.13 shows the energy resolution for 50 GeV K_L^0 as a function of number of layers in the HCal. As the number of layers in the HCal is increased, the energy resolution improves. This is because increasing the number of layers in a sampling calorimeter, while leaving the total material budget unchanged, will lead to greater sampling of particles showering within it and a reduction the stochastic contribution to the energy resolution. The energy resolution is less pronounced than the naive expectation of $1/N_{\text{HCal}}$, where N_{HCal} is the number of layers in the HCal, because this relationship only holds for the energy resolution of a single sampling calorimeter and these results are for the full ILD detector, including the $\approx 1\lambda_I$ in the ECal. Furthermore, the $1/N_{\text{HCal}}$ functional form neglects a number of effects, such as instrumentation defects and electrical noise, that should be included when parameterising the energy resolution [5].
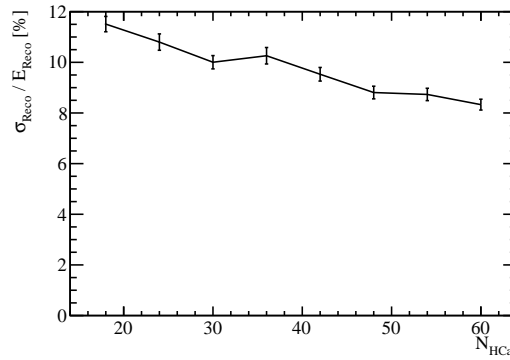

Figure 1.13: The energy resolution as a function of the longitudinal sampling frequency in the HCal for 50 GeV K_L^0 events using the nominal ILD detector model.

Figure 1.14 shows the jet energy resolution as a function of the longitudinal sampling frequency in the HCal. Increasing the number of layers in the HCal leads to an improvement in the HCal; when the number of layers in the HCal is increased 18 to 60 the jet energy resolution for 250 GeV jets improves by $\sim 17\%$.

Figure 1.15 shows that both the intrinsic energy resolution and confusion improve with increasing longitudinal sampling frequency. The twofold improvement is expected because increasing the longitudinal sampling frequency improves the intrinsic energy resolution of a sampling calorimeter, which has the knock-on effect of lowering the confusion. Improving the intrinsic energy resolution of a calorimeter reduces confusion because it means more precise comparisons can be made between the momenta of charged particle tracks and the energy of clusters of calorimeter hits. These comparisons are used to guide event reconstruction in PandoraPFA, therefore, if the precision of the comparisons is improved confusion is reduced as described in section **??**.
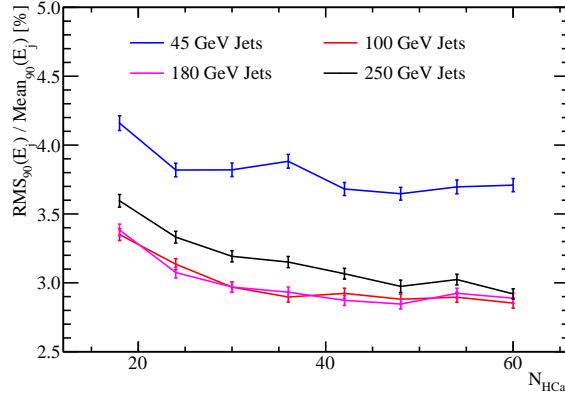
Figure 1.14: The jet energy resolution as a function of longitudinal sampling frequency in the HCal for various jet energies using the nominal ILD detector model.
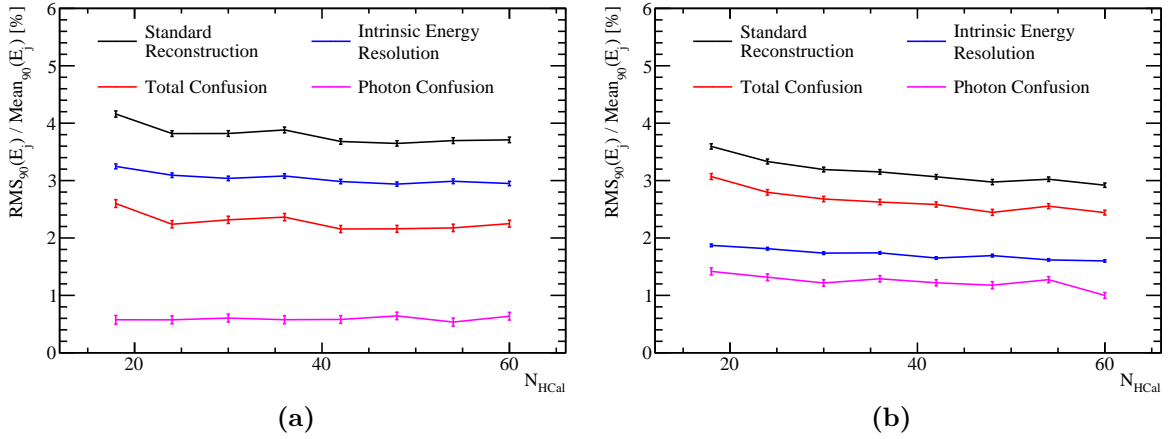

Figure 1.15: The contributions to the jet energy resolution as a function of the longitudinal sampling frequency in the HCal using the nominal ILD detector model for (a) 45 GeV jets and (b) 250 GeV jets. The black curves correspond to the standard reconstruction, the blue curves to the intrinsic energy resolution contribution to the jet energy resolution, the red curves to the confusion contribution to the jet energy resolution and the magenta curves to the confusion contribution to the jet energy resolution related solely to γ reconstruction.

It is clear that a larger number of layers in the HCal benefits both the intrinsic energy resolution of the ILD detector as well as reducing the confusion contribution to the jet energy resolution. As there are few physics analyses that rely on the identification and categorisation of individual neutral hadrons, but there are many that rely on identification and categorisation of γs, the intrinsic energy resolution of the HCal is less crucial from a physics perspective than that of the ECal. However, these studies show the HCal has a crucial role to play in jet reconstruction in the particle flow paradigm. To achieve a jet energy resolution of $\sigma_E/E \lesssim 3.8\%$, which is required to separate the W and Z

hadronic decays, the ILD detector will require a minimum of 42 layers in the HCal. This longitudinal sampling frequency is required particularly for low energy jets where the energy resolution is dominated by the intrinsic energy resolution of the detector.

1.3.4 HCal Sampling Fraction

The performance of the ILD detector was studied for different ratios of active to absorber later thicknesses in the HCal. In the nominal detector model, the active scintillator layer thickness is 3 mm, while the absorber layer thickness is 20 mm giving a sampling fraction of 0.15. HCal models were simulated where this ratio was changed from 0.05 to 0.25 in steps of 0.05, while retaining the same number of interaction lengths.

No performance changes in the energy resolution for 50 GeV K_L^0s or the jet energy resolution for 91, 200, 360 and 500 GeV Z→uds di-jet events were observed when varying the ratio of active to absorber later thicknesses. Based on these simulations, there is no suggestion that varying this ratio has any statistically significant effect on the physics performance, however, ...

This indicates the particle showers are sufficiently well sampled in all detector models considered and that thinning the active layer of the ILD HCal down to ~ 1 mm would not harm the detector performance.

1.3.5 HCal Absorber Material

The nominal choice of HCal absorber material is steel with tungsten providing a feasible alternative [6]. Although tungsten is more expensive than steel, it contains a larger number of nuclear interaction lengths per unit length. Therefore, using tungsten as the absorber material would allow for a reduction in the size of the HCal, while retaining the same number of nuclear interaction lengths. Reducing the depth of the calorimeter would decrease the size of the solenoid required, which would offset some of the additional cost if tungsten were to be used.

The configuration for the steel and tungsten HCal options that were used in the full ILD simulation can be found in table 1.5. To isolate the effects of changing the absorber material, the total depth, in nuclear interaction lengths, was kept constant when comparing the two options. Furthermore, the sampling fraction was also held constant. A number of different physics lists exist within GEANT4 for the modelling of hadronic

showers. The default model for high energy physics calorimetry is the QGSP_BERT physics list. This uses the quark-gluon string model [7] with the precompound model of nuclear evaporation [8] (QGSP) for high energy interactions and the Bertini (BERT) cascade model [9] for intermediate energy interactions. For the study of absorber materials both the QGSP_BERT and the QGSP_BERT_HP physics lists were used. The QGSP_BERT_HP list uses the high precision neutron package (NeutronHP) to deal with the transportation of neutrons from below 20 MeV to thermal energies. This added detail is necessary for accurate modelling of hadronic showers in tungsten [10].

Parameter	Steel HCal Option	Tungsten HCal Option
Cell Size	30×30 mm^2 square cells	30×30 mm^2 square cells
Number of Layers	48 readout layers	48 readout layers
Absorber Material Thickness [mm]	20.0	12.0
Active Material Choice	Scintillator	Scintillator
Active Material Thickness [mm]	3.0	1.8

Table 1.5: The configuration of the steel and tungsten HCal options [1].

One of the dominant processes governing the energy deposition of hadronic showers in calorimeters is spallation [11]. Spallation begins with the collision of a high energy incident particle with nucleons in the calorimeter absorber material. This collision creates a cascade of high energy hadronic particles, e.g. protons, neutrons and pions, are produced within the nucleus. If these energies are large enough, some of these particles may escape the nucleus and form secondary particles in the hadronic shower. After this initial collision, the nuclei of the absorbing material are left in an excited state. Assuming the excited nuclei are sufficiently stable that they will not undergo fission, they will return to a stable state by ejecting energy in the form of particles in a process called evaporation. Evaporation of neutrons, which is the dominant form of evaporation, significantly delays the growth of hadronic showers as after the evaporation process some of these neutrons participate in neutron capture [10]. Neutron capture involves an absorber nuclei capturing a neutron and then emitting a γ as it returns to a stable state. The time taken for the neutron capture mechanism to proceed is limited by the lifetime of the unstable nuclei [12], which typically makes neutron capture one of the slowest mechanisms by which hadronic showers can propagate. The number of evaporation neutrons released in a hadronic shower grows as the atomic number, Z, of the absorber material of a calorimeter increases. This is because of the increase in neutron content

of the absorber material nuclei [10]. As the number of evaporation neutrons increases, more neutron capture processes are initiated, which results in a longer hadronic shower development time. Figure 1.16 shows the shower development times for hadronic showers in the tungsten (Z=74) and steel (iron, Z=26) HCal options and, as expected, the shower development time is greater for tungsten.
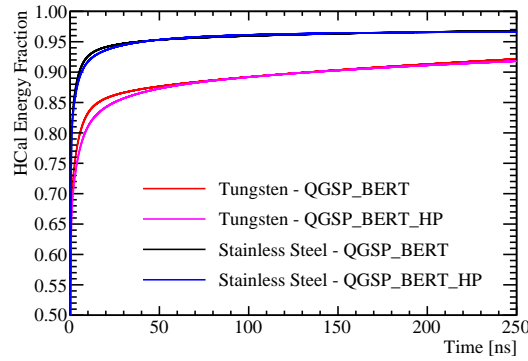

Figure 1.16: The fraction of the total calorimetric energy deposited in the HCal as a function of time for 25 GeV K_L^0 events using the steel and tungsten HCal options. Results are shown for both the QGSP_BERT and QGSP_BERT_HP physics lists. The calorimeter hit times have been corrected for straight line time of flight to the impact point.

Table 1.6 shows the energy resolution for 50 GeV K_L^0s obtained using the nominal ILD detector model with various HCal absorber materials and GEANT4 physics lists. The tungsten HCal option offers a slight improvement over steel in the energy resolution. This can be attributed to differences in the nuclear structure of the two materials, which will lead to different developments of the hadronic showers within them. For example, the energy losses to nuclear binding energies are smaller in tungsten than steel, as the target nucleons are less stable than in iron, therefore, less energy is needed to liberate them. This will lead to a larger signal for tungsten and a reduction in the energy resolution in comparison to steel. The results of table 1.6 also indicate that the addition of the high precision neutron package was not important for this study.

It should be emphasised that the HCal hit energy truncation, as described in chapter **??**, used for the tungsten and steel HCal options differs because tungsten contains a larger number of radiation lengths per nuclear interaction length than steel does. As the HCal primarily measures hadronic showers, one may naively expect the number of radiation lengths in the HCal to be irrelevant, given both options have the same number of nuclear interaction lengths. However, this is not the case as all hadronic showers have

HCal Option	Energy Resolution [%]
Steel, QGSP_BERT	8.8 ± 0.2
Steel, QGSP_BERT_HP	9.0 ± 0.3
Tungsten, QGSP_BERT	8.3 ± 0.2
Tungsten, QGSP_BERT_HP	8.3 ± 0.2

Table 1.6: The energy resolution for 50 GeV K_L^0s obtained using the nominal ILD detector with various HCal absorber materials and GEANT4 physics lists.

an electromagnetic component generated by the decays of hadrons to γs, e.g $\pi^0 \to \gamma\gamma$ and $\eta \to \gamma\gamma$. This leads to hadronic showers depositing more energy per calorimeter hit in tungsten than in steel and makes retuning the HCal hit energy truncation a necessity. As expected, the truncation used for tungsten, 5 GeV, is larger than for steel, 1 GeV, because of the increased average hit energy.

Table 1.7 shows the jet energy resolutions for selected jet energies obtained using the nominal ILD detector with various HCal absorber materials and GEANT4 physics lists. These results indicate that steel outperforms tungsten as the absorber material for the HCal. As the jet energy increases, the magnitude of the difference in jet energy resolutions between the two options grows. This indicates the differences in jet energy resolution between the two options is driven by the confusion contribution as this contribution grows with increasing jet energy. Furthermore, as the K_L^0 energy resolution was only slightly better for the tungsten option, it is expected that the intrinsic energy resolution contribution to the jet energy resolution will not vary significantly between the two as only a small fraction of jet energy is measured in the HCal. The intrinsic energy resolution and confusion contributions to the jet energy resolution for 45 and 250 GeV jets are shown in table 1.8. As expected, the intrinsic energy resolution contribution to the jet energy resolution is nearly identical for the various options. However, the confusion contribution to the jet energy resolution is larger for the tungsten HCal option than for the steel HCal option.

This is due to the PandoraPFA algorithms being tuned for the nominal (steel) ILD HCal dimensions, while the cells for the alternative tungsten option are thinner by a factor of approximately $\lambda_I^{Steel}/\lambda_I^{Tungsten} \approx 1.7$, where λ_I^x is the radiation length in material x. It is unfeasible to tune all of the PandoraPFA algorithms to each detector geometry, however, the breakdowns of the jet energy resolution indicate that even if this were done, the tungsten option would offer no advantage to the steel option in terms of intrinsic

energy resolution. Once again, it was noted that the use of the QGSP_BERT_HP physics list, as opposed to QGSP_BERT, made a minimal impact on these results.

	Jet Energy Resolution [%]			
HCal Option	45 GeV	100 GeV	180 GeV	250 GeV
Steel, QGSP_BERT	3.65 ± 0.05	2.88 ± 0.04	2.85 ± 0.04	2.97 ± 0.05
Steel, QGSP_BERT_HP	3.67 ± 0.05	2.92 ± 0.04	2.86 ± 0.04	3.03 ± 0.04
Tungsten, QGSP_BERT	3.78 ± 0.05	3.12 ± 0.04	3.15 ± 0.04	$3.43 \pm 0.04|$
Tungsten, QGSP_BERT_HP	3.80 ± 0.05	3.08 ± 0.04	3.24 ± 0.04	3.41 ± 0.04

Table 1.7: The jet energy resolution for selected jet energies obtained using the nominal ILD detector with various HCal absorber materials and GEANT4 physics lists.

	Jet Energy Resolution [%]			
	45 GeV		250 GeV	
HCal Option	Intrinsic	Confusion	Intrinsic	Confusion
Steel, QGSP_BERT	2.93 ± 0.04	2.16 ± 0.06	1.69 ± 0.02	2.45 ± 0.05
Steel, QGSP_BERT_HP	2.98 ± 0.04	2.15 ± 0.06	1.65 ± 0.02	2.53 ± 0.04
Tungsten, QGSP_BERT	2.97 ± 0.04	2.34 ± 0.06	1.65 ± 0.02	3.01 ± 0.05
Tungsten, QGSP_BERT_HP	2.92 ± 0.04	2.42 ± 0.06	1.65 ± 0.02	2.99 ± 0.05

Table 1.8: The contributions to the jet energy resolution obtained using the nominal ILD detector with various HCal absorber materials and GEANT4 physics lists.

In conclusion, there are no large differences in the intrinsic energy resolution of the ILD detector simulation, for either neutral hadrons or jets, when changing the HCal absorber material from steel to tungsten. The steel option HCal outperforms the tungsten option in terms of pattern recognition confusion, when using the default PandoraPFA settings, although this could be addressed should it become clear that tungsten were a preferred option. However, when examining the mechanical properties of steel and tungsten, it is clear that steel has a significant advantage over tungsten in terms of rigidity [13]. This means that fewer support structures would be required for the calorimeter leading to less dead material and better performance, which makes steel more preferred option.

1.4 Global Detector Parameters

The detector geometry and the magnetic field strength are major cost drivers for the ILD detector. Both will have an affect on the jet energy resolution and, for completeness, studies showing their impact on detector performance are presented here.

1.4.1 The Magnetic Field Strength

In the particle flow paradigm the momentum of charged particles is obtained through the curvature of the track they traverse as they bend in the magnetic field. Therefore, the magnetic field is an integral element for the successful application of particle flow calorimetry. Furthermore, the magnetic field deflects charged particles away from neutral particles in jets. The stronger the magnetic field, the larger the separation between the calorimetric energy deposits made by charged and neutral particles in jets, which reduces the effect of confusion. Therefore, it is expected that a stronger magnetic field will lead to better jet energy resolutions through a reduction of the confusion contribution to the jet energy resolution.

Detector models were simulated where the magnetic field was varied from 1 to 5 T in steps of 0.5 T and the jet energy resolutions for these detectors is shown in figure 1.17. For high energy jets there is a strong trend whereby a stronger magnetic field leads to a better jet energy resolution. While, at low jet energies the jet energy resolution is almost invariant to changes in the magnetic field.
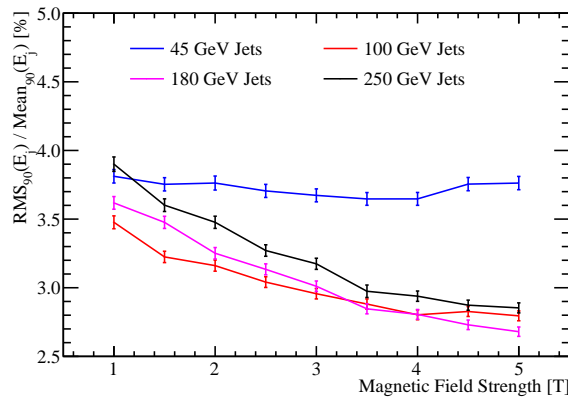

Figure 1.17: The jet energy resolution using the nominal ILD detector as a function of the magnetic field strength for various jet energies.

The jet energy resolution breakdowns into the various contributions are shown in figure 1.18 and as expected there is clear reduction in the confusion contribution to the jet energy resolution with increasing magnetic field strength. Furthermore, there is a reduction in intrinsic energy resolution with increasing magnetic field strength for low energy jets. At low energies, the radius of curvature of the helix charged particles traverse will be small. If the radius for a given particle is small enough, the particle will not enter the calorimeters. In this case, only if the track produced from this particle passes tight selection cuts, designed to ensure the track originates from the IP, will the track be used in the reconstruction. Therefore, energy can and will be lost from events where particles are stuck within the tracker. Given the radii of curvature is inversely proportional to the magnetic field strength, the larger the magnetic field strength the more tracks will be confined to the tracker as is shown by figure 1.19. The more tracks that are confined to the tracker, the worse the intrinsic energy resolution becomes as inevitably some tracks fail the quality cuts. At high jet energies, low transverse momentum charged particles will still get trapped within the tracker, however, these contribute fractionally little energy to the total reconstructed energy. Therefore, the trend of worsening intrinsic energy resolution with increasing magnetic field strength is less pronounced as the jet energy grows. At very low magnetic field strengths and high jet energies, the intrinsic energy resolution actually degrades, due to an artefact in the determination of the intrinsic energy resolution. The intrinsic energy resolution is determined by associating a single MC particle to each calorimeter cell. At low magnetic field strengths and high jet energies, many of the MC particles will have overlapping energy deposits within the calorimeter cells and so associating a single MC particle per cell is inaccurate. This leads to imperfect association of charged particle tracks to calorimetric energy deposits, which worsens the intrinsic energy resolution. However, as this effect is second order small in comparison to changes in the confusion contribution the overall dependancy of detector performance on the magnetic field strength can be confidently quantified.

In summary, increasing the magnetic field strength is beneficial to detector performance as it reduces confusion from associating tracks to calorimetric energy deposits from charged particles. While there is a reduction in the intrinsic energy resolution for low transverse momentum jets with increasing magnetic field strength, this effect is largely offset by the change in confusion. While the nominal field of 3.5 T gives good performance increasing the field strength is a clear way of making gains in detector performance.
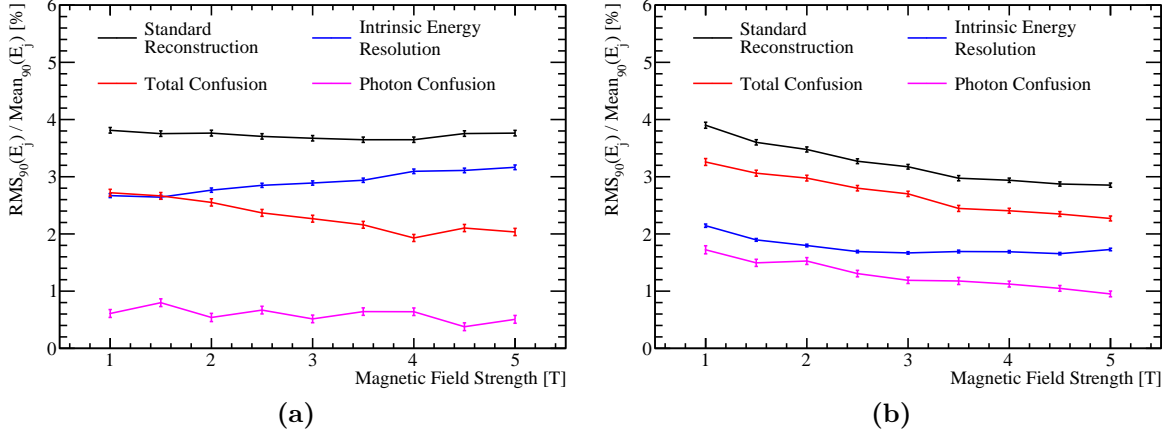
Figure 1.18: The contributions to the jet energy resolution as a function of the magnetic field strength using the nominal ILD detector model for (a) 45 GeV jets and (b) 250 GeV jets. The black curves correspond to the standard reconstruction, the blue curves to the intrinsic energy resolution contribution to the jet energy resolution, the red curves to the confusion contribution to the jet energy resolution and the magenta curves to the confusion contribution to the jet energy resolution related solely to γ reconstruction.
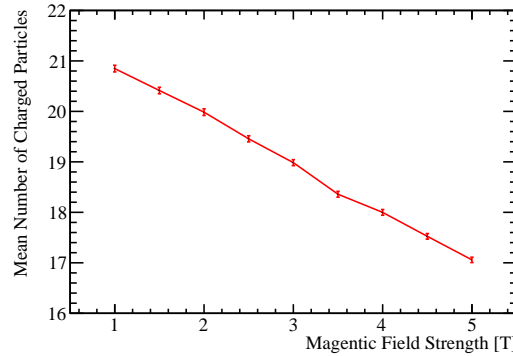

Figure 1.19: The mean number of reconstructed charged particles as a function of the magnetic field strength for 91 GeV Z→uds di-jet events. The nominal ILD detector model was used and the pattern recognition has been fully cheated using the MC information.

1.4.2 Inner ECal Radius

Detector models were considered where the ECal inner radius was set to 1208, 1408, 1608, 1808 (nominal) and 2008 mm. For these models, all other detector parameters were identical to those found in the nominal ILD detector model.

Figure 1.20 shows the dependence of the jet energy resolution on the ECal inner radius. The simulations indicate that a large ECal inner radius was highly beneficial to detector performance, which is due to the increase in the time it takes for particles to reach the calorimeters. The longer it takes for the particles to reach the calorimeters the more the charged particles will bend in the magnetic field and the larger separation will be between calorimetric energy deposits from charged and neutral particles. This larger this separation the smaller the effect of confusion. This conclusion is backed up by the decomposition of the jet energy resolution, shown in figure 1.21. These results explicitly show a reduction in confusion with increasing ECal inner radius. The intrinsic energy resolution of the detectors shows no strong dependence on the inner ECal radius. There is a small degradation in intrinsic energy resolution at low ECal inner radii, which is due to the association of a single MC particle per calorimeter cell when running the cheated pattern recognition as explained in section 1.4.1. Again, this effect has little bearing on the final conclusions as the change in intrinsic energy resolution across the detector models is a second order effect.
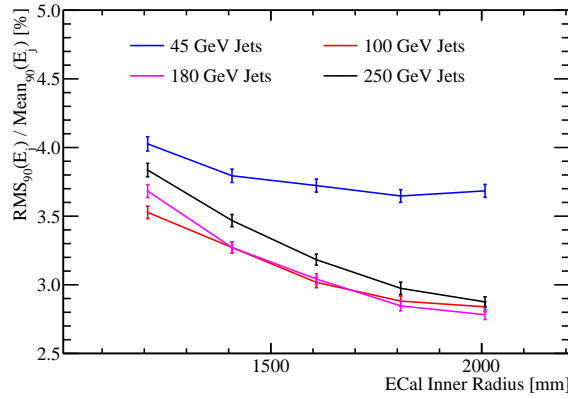

Figure 1.20: The jet energy resolution using the nominal ILD detector as a function of the ECal inner radius for various jet energies.

In conclusion, increasing the ECal inner radius benefits the jet energy resolution significantly. This trend is driven by changes to the confusion in associating calorimetric energy deposits to charged particle tracks.
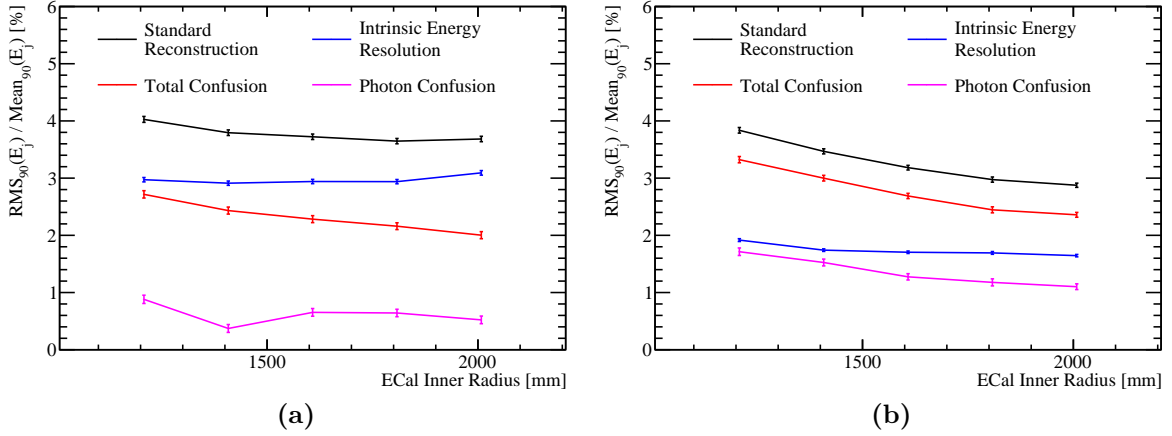
Figure 1.21: The contributions to the jet energy resolution as a function of the ECal inner radius using the nominal ILD detector model for (a) 45 GeV jets and (b) 250 GeV jets. The black curves correspond to the standard reconstruction, the blue curves to the intrinsic energy resolution contribution to the jet energy resolution, the red curves to the confusion contribution to the jet energy resolution and the magenta curves to the confusion contribution to the jet energy resolution related solely to γ reconstruction.

Colophon

This thesis was made in LaTeX 2_ε using the "hepthesis" class [14].

Bibliography

[1] Halina Abramowicz et al. The International Linear Collider Technical Design Report - Volume 4: Detectors. 2013.

[2] Toshinori Abe et al. The International Large Detector: Letter of Intent. 2010.

[3] C. Patrignani et al. Review of Particle Physics. *Chin. Phys.*, C40(10):100001, 2016.

[4] J. B. Birks. Scintillations from Organic Crystals: Specific Fluorescence and Relative Response to Different Radiations. *Proc. Phys. Soc.*, A64:874–877, 1951.

[5] C. W. Fabjan and F. Gianotti. Calorimetry for particle physics. *Rev. Mod. Phys.*, 75:1243–1286, 2003.

[6] M. Chefdeville et al. Shower development of particles with momenta from 15 GeV to 150 GeV in the CALICE scintillator-tungsten hadronic calorimeter. *JINST*, 10(12):P12006, 2015.

[7] G. Folger and J. P. Wellisch. String parton models in GEANT4. *eConf*, C0303241:MOMT007, 2003.

[8] *Geant4 Physics Reference Manual, Section IV, Chapter 28.*

[9] M. P. Guthrie, R. G. Alsmiller, and H. W. Bertini. Calculation of the capture of negative pions in light elements and comparison with experiments pertaining to cancer radiotherapy. *Nucl. Instrum. Meth.*, 66:29–36, 1968.

[10] C. Adloff et al. The Time Structure of Hadronic Showers in highly granular Calorimeters with Tungsten and Steel Absorbers. *JINST*, 9:P07022, 2014.

[11] R. Wigmans. Calorimetry: Energy measurement in particle physics. *Int. Ser. Monogr. Phys.*, 107:1–726, 2000.

[12] A. Caldwell, L. Hervas, J. A. Parsons, F. Sciulli, W. Sippach, and L. Wai. Measurement of the time development of particle showers in a uranium scintillator

calorimeter. *Nucl. Instrum. Meth.*, A330:389–404, 1993.

[13] Lucie Linssen, Akiya Miyamoto, Marcel Stanitzki, and Harry Weerts. Physics and Detectors at CLIC: CLIC Conceptual Design Report. 2012.

[14] Andy Buckley. The hepthesis LaTeX class.